Material Scrunching Enables Working Channels in Miniaturized Vine-Inspired Robots

Cédric Girerd[1,2], Anna Alvarez[3], Elliot W. Hawkes[3], and Tania K. Morimoto[1,4], *Senior Member, IEEE*

***Abstract*—A new subclass of soft robot, known as tip-extending or "vine" robots, consists of long inflatable devices that move through the environment by extending from the tip. A key requirement for many applications of these robots is a working channel—a hollow tube through the core of the robot for passing tools, sensors, fluids, etc. While working channels have been proposed in a few vine robots, it remains an open challenge to create miniaturized vine robots (diameter < 1 cm) with working channels that enable continuous access through the core. In this paper, we analyze the growth models of current vine robot designs and show that the working channel greatly increases required pressure to grow at small scales due to internal friction. Based on this insight, we propose the concept of storing scrunched material at the tip of the vine robot to circumvent this frictional force. We validate our models and demonstrate this concept via prototypes down to diameters of 2.3 mm. Overall, this work enables the creation of miniaturized vine robots with working channels, which significantly enhances their practicality and potential for impact in applications such as minimally invasive surgery.**

***Index Terms*—Soft robots, Bio-inspired robots, Robot design.**

I. Introduction

SOFT growing robots, or vine robots, have demonstrated significant potential for applications involving human-robot interactions, navigation through highly constrained paths, and exploration in fragile environments. These robots are characterized by their long, flexible, inflatable body and method of movement via tip extension, driven by internal body pressure [1], [2], [3], [4], [5]. In contrast to traditional continuum and soft robots that must translate relative to the environment in order to achieve forward motion, an internal pressure causes new material (the "tail") to extend from the tip of these robots, lengthening their body in a manner that resembles the growth of vines. To date growing robots tend to be on the order of $5-10$ cm in diameter, with deployed lengths on the order of meters, in some cases. These robots have been designed for exploration of archaeological sites [6], creation of reconfigurable antennas [7], navigation through coral reefs [8], and burrowing through granular media [9].

This work was supported in part by the National Science Foundation under Grant 1935329 and Grant 1944816, in part by the Packard Foundation, and in part by the National Institute of Health under Grant 13499720.

[1]Department of Mechanical and Aerospace Engineering, University of California, San Diego, La Jolla, CA 92093 USA (e-mail: cgirerd@eng.ucsd.edu (corresponding author)).

[2]LIRMM, Univ Montpellier, CNRS, Montpellier, France.

[3]Department of Mechanical Engineering, University of California, Santa Barbara, CA 93106 USA (e-mail: anna_alvarez@umail.ucsb.edu, ewhawkes@engineering.ucsb.edu).

[4]Department of Surgery, University of California, San Diego, La Jolla, CA 92093 USA. (e-mail: tkmorimoto@eng.ucsd.edu).

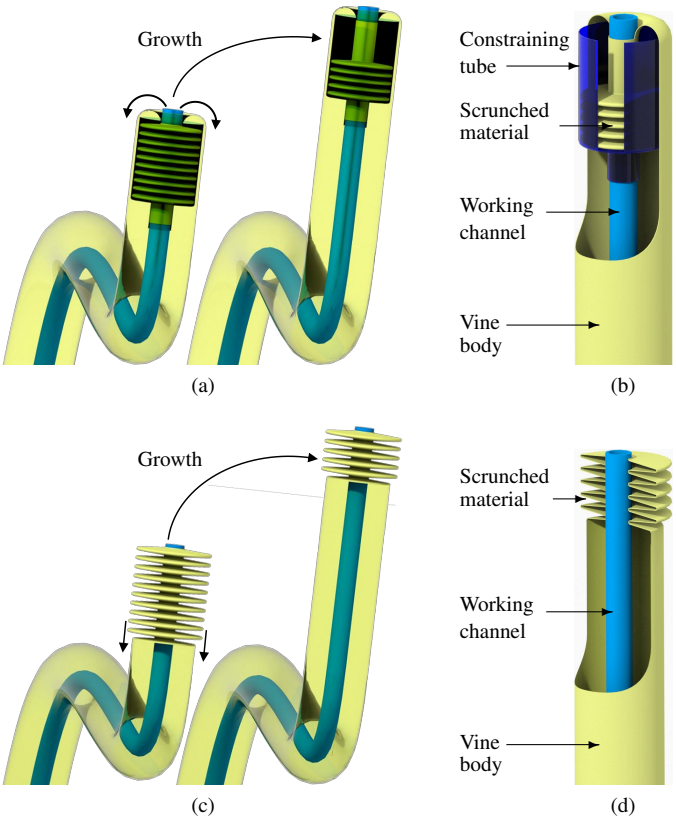

Fig. 1. Illustration of two new vine robot designs that overcome scaling limitations of current designs with working channels via our proposed concept of material scrunching. (a) Our proposed everting scrunched design is shown at two different steps during deployment, along with (b) a zoomed-in view of the tip. (c) Our proposed non-everting scrunched design is shown at two steps during deployment, along with (d) a zoomed-in view of the tip.

Despite the numerous potential benefits of growing robots, current designs are impractical for many applications for two main reasons. First, current designs are often too large, or cannot grow far enough along curved paths. There are several applications—including medical and inspection tasks, for example—that could benefit from the advantages offered by vine robots, but require millimeter-scale devices. Second, vine robots must be equipped with the proper tools in order to perform the desired task, which is challenging due to the robot structure and mechanism of growth. We propose to overcome these current limitations of vine robots with two new designs, visible in Fig. 1.

To date there have been several proposed approaches to tool integration. One such solution has been to create a mount that sits at the tip of the robot [10], [11], [6]. This approach has

been successfully demonstrated for grippers and cameras, but it can pose challenges with regards to wire management, can result in heavy loads at the tip [12], and is insufficient for applications that require the ability to pass tools or materials from the robot base to the tip in order to gain access to the outside environment. Another approach has therefore been to use the space inside the tail of the vine robot [13], [14]. However, since the tail translates at twice the speed of the robot tip, any tool inside the tail must be actively translated backward with respect to the tail to remain at a desired location (the tip of the vine robot). And because the internal pressure causes the tail to press on any element located inside, this relative motion is difficult.

An alternative approach, has been to instead integrate a "working channel"—a radially rigid, hollow tube, through which any tool can be passed from the robot base to tip. To date there have been several design architectures for integrating a working channel. The first design consists of placing the working channel inside the tail material, and because it is radially rigid, it is able to withstand the pressure and remain a hollow access channel for tools. However, in order to prevent the working channel from being pushed past the tip of the vine robot as the tail material moves forward, it must be moved backward with respect to the tail. The large pressures required to overcome the friction between the working channel and the tail, however, can lead to bursting. In [14], [13], a "duty cycle controller", which alternates pressurizing/depressurizing the vine robot, has been adopted to solve this issue. However, this duty cycle approach results in a significant decrease in speed. Another approach is to blow air between the working channel and the vine robot tail, in order to limit friction forces between them [9]. This is, however, impractical for medical applications, for example, since it can lead to leaks at the robot tip. Finally, in our previous work we investigated a design with the tail and working channel in-line [15]. This design enables the elimination of the friction forces between the vine robot tail and the working channel. However, this design only allows for tool access at the very end of deployment. Therefore, while there have been demonstrations of vine robots on the order of around 3 mm, creating small-scale vine robots with working channels that allow tool access at all points of deployment during continuous growth, especially over long deployment lengths, remains an open challenge.

We seek to overcome the limitations in the miniaturization of vine robots with working channels in order to enable their use in environments and applications that are currently infeasible. Specifically, the contributions of this work are as follows. First, we analyze the impact of the vine robot design parameters on their scaling, and, in particular, on their miniaturization with the inclusion of a working channel. These impacts are determined through analysis of the growth model of these robots, in the case of straight and curved paths. Second, we propose two new vine robot designs based on the concept of storing scrunched material at the tip of the robot that overcome current scaling limitations of vine robots with working channels (Fig. 1). These designs enable miniaturization of vine robots with working channels that allow tool access at all points of deployment during continuous growth at scales not currently possible. Third, we experimentally evaluate the performance of our proposed vine robot designs and validate their associated models. These experiments highlight the significant potential benefits of our new vine robot designs for applications in small, highly constrained, sensitive environments.

The rest of the paper is structured as follows: Section II presents the current vine robot designs and models, highlighting their growth limits as they are scaled down. In Section III, we present new vine robot designs, based on material scrunching, that allow us to overcome these limits. We experimentally evaluate our proposed designs in Section IV. Finally, we present conclusions and perspectives of this work in Section V.

II. Vine Robot Scaling

In this section, we present an overview of vine robots in terms of their working principle and modeling. We then analyze the limits of current designs as their cross sections are isometrically scaled, highlighting the key challenges for miniaturizing vine robots with working channels. The key result, which we show below, is that as vine robots with working channels are scaled down in diameter, they require higher pressures to grow.

A. General Vine Robot Modeling

Soft growing robots are made from an inextensible, thin-walled material that is formed into a tube. One approach for achieving tip-extension, is to invert one end of the robot material back inside the main body. This inverted material—often called the "tail" of the vine robot—then everts from the robot tip when an internal pressure is applied. The modeling of such vine growing robots has been inspired by growing plants and was initially presented in [16]. This model was then extended in [14] to include a working channel (see Fig. 2, *top*), and is obtained through a quasi-static analysis of forces acting on the vine robot tail. Without any model simplifications, for a vine robot with radius, R, and a working channel with radius, r, the growth model is given as follows:

$$\underbrace{\frac{1}{2}P_{grow}\pi(R^2-r^2)}_{\text{Driving Force}} = \underbrace{\left[\frac{1}{2}F_y + \left(\frac{1}{\varphi}v\right)^{\frac{1}{n}}\pi(R^2-r^2)\right]}_{\text{Path-Independent Opposing Forces}} + \underbrace{\left[\mu_{\text{VT/WC}}P_{grow}2\pi rL + \mu_{\text{VT/VB}_s}wL + Ce^{\mu_{\text{VT/VB}_c}\Gamma}\right]}_{\text{Path-Dependent Opposing Forces}}, \quad (1)$$

in the case where the working channel translates at a slower speed than the vine tail, which is required to keep it at the tip of the robot. The variables are defined below. On the left-hand side of the equation is the driving force, which leads to growth. This term describes the growth force related to the internal pressure of the vine robot, P_{grow}, applied to its cross section (represented in green in Fig. 2). On the right-hand side of Eq. (1) are the forces opposing growth, and these can be classified as path-independent and path-dependent forces. The first path-independent term, $\frac{1}{2}F_y$, characterizes the

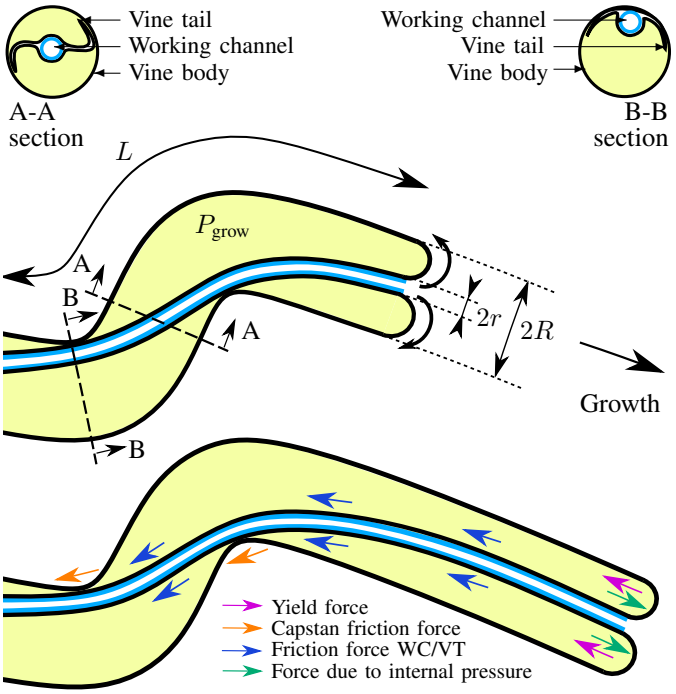

Fig. 2. Illustration of a vine growing robot with a working channel at two different growth stages, with its design parameters represented in the top configuration and a free body diagram illustrating the forces from Eq. (2) in the bottom configuration. The A-A cross-section illustrates the contact between the vine robot tail and its body in straight path, with the tail and working channel remaining mostly centered inside the vine body, and the B-B cross-section illustrates the contact area between the vine robot tail and its body in curved path, with the working channel and vine tail touching the inside of the curved vine body.

yield force required for material eversion at the tip, and is represented in pink in Fig. 2. The second path-independent term is velocity dependent and models viscoplastic effects as the deployment speed at the vine robot tip, v, increases, where φ is an extensibility term and n is a coefficient close to unity [17]. The first path-dependent term models the friction between the vine robot tail and the working channel. Indeed, the working channel needs to travel at half the speed of the tail to be aligned with the vine robot tip [16]. Thus, a relative motion between the tail and the working channel is required, and friction forces between them must be overcome. Since we consider working channels that have cylindrical cross-sections, their surface area is equal to $2\pi rL$. The normal force exerted by the vine robot tail on the working channel is $P_{grow}2\pi rL$, and the tangential force (represented in blue in Fig. 2) is obtained by multiplying by the friction coefficient between the working channel and vine tail materials ($\mu_{\text{VT/WC}}$), leading to $\mu_{\text{VT/WC}}P_{grow}2\pi rL$. We note that if the working channel translates at the same speed as the vine tail, the term $\mu_{\text{VT/WC}}P_{grow}2\pi rL$ vanishes, and if the working channel translates at a faster speed than the vine tail, it becomes a driving force. These modes of deployment, however, would lead to the working channel passing the eversion point of the vine material, which is not a desired behavior in our work. The second path-dependent term models the friction between the tail and the body of the robot in straight paths, where $\mu_{\text{VT/VB}_s}$ is the friction coefficient between the tail and body materials, and w is the unit force exerted by the tail on the vine robot body. The third path-dependent term corresponds to added friction in curved parts of the vine robot body (represented in orange in Fig. 2), where tension in the tail due to pressure at the vine robot tip presses the tail towards the inside of the curved vine robot body. In this term, C is a tension force, $\mu_{\text{VT/VB}_c}$ is the friction coefficient between the tail and body materials due to curvature, and Γ is the total angle swept by all turns of the path. In the remainder of the paper, we refer to this vine robot design with a working channel through the tail [14] as the "standard" design.

Starting with the general model given by Eq. (1), we then make the following assumptions. First, we consider the relatively slow growth case such that the velocity-dependent term in Eq. (1) is negligible. In addition, the friction force between the vine robot tail and its body along straight paths is very small compared to the other contributors in Eq. (1). With these assumptions, Eq. (1) becomes:

$$\frac{1}{2}P_{grow}\pi(R^2-r^2)=\frac{1}{2}F_y+\mu_{\text{VT/WC}}P_{grow}2\pi rL+Ce^{\mu_{\text{VT/VB}_c}\Gamma}. \tag{2}$$

We note that in this quasi-static case, where the growth speed of the robot is low, we assume that the compressibility of the media used inside the vine does not play a role in the robot behavior, and either air or water could be used [5], [15].

B. Scaling and Growth Length Limitations

Because we are interested in the design of miniaturized vine robots (small diameters) with relatively long lengths, we first analyze the growth limitations as vine robots are isometrically scaled in the radial direction (i.e. r/R and t/R fixed). To do so, we rearrange Eq. (2) to solve for the growth pressure, which must be below the burst pressure for viable growth. To help with analysis, we seek to understand how all terms scale as the size of the vine robot changes. In particular, for the yield force, F_y, previous work found that it is independent of the robot cross-sectional area [16]. However, through experimentation, we found that it depends on the thickness of the vine body material approximately as $F_y = kt^2$ for low density polyethylene (LDPE) (see Appendix A for details), where t is the thickness of the vine material and k is an empirically determined constant. In this work, the tension force C in the Capstan force is assumed to be scale-independent. Eq. (2) can then be rewritten in order to obtain the growth pressure, P_{grow}, of a vine robot, and is given as:

$$P_{grow}=\frac{kt^2+Ce^{\mu_{\text{VT/VB}_c}\Gamma}}{\pi(R^2-r^2)-\mu_{\text{VT/WC}}4\pi rL}. \tag{3}$$

We note that our model in Eq. (3) is receptive to other materials if future work characterizes their yield forces. Using Eq. (3), one can assess the change in growth pressure as vine robots are scaled. For $\alpha \in [0,1]$, $P_{grow}(\alpha R,\alpha r,\alpha t) \geq P_{grow}(R,r,t)$, and thus vine robots that are scaled down require a larger pressure to grow. Equivalently, this means that for a given pressure, scaled vine robots can only grow for a shorter length.

To understand this result, we note that the pressure will tend towards infinity as the second term $\mu_{\text{VT/WC}} 4\pi r L$ in the denominator of Eq. (3) approaches the first term $\pi(R^2 - r^2)$. While the first term in the numerator and the first term in the denominator depend on the square of the scale, the second term in the denominator depends linearly. This means that the second term, which represents the internal friction between the tail and the working channel, will become relatively larger during down-scaling and must be mitigated to enable small-scale vine robots with working channels. Lastly, the second term in the numerator, which represents the capstan friction in the presence of curves, is scale-independent, meaning that as a vine robot is scaled down, the additional pressure required to grow through a curved path compared to a straight path increases, such that down-scaling vine robots is more limited when curves are added to the path.

Fig. 3 shows this increase in growth pressure for a vine robot as its cross section is scaled down, for the case of both curved (dotted lines) and straight (solid line) paths. The robot selected has the following parameters: $r/R = 0.1$, $\mu_{\text{VT/WC}} = 0.1$, material is LDPE with $t/R = 0.005$. For simulations along curved paths, we consider $\mu_{\text{VT/VB}_c} = 0.22$ and $C = 0.08$ as estimated in [18]. We define the radius of curvature of the path to be 12 mm such that the vine robot shape does two full revolutions for the longest deployed length considered ($L = 150$ mm). The burst pressure was estimated by pressurizing 5 LDPE tubes of diameter 31.8 mm and thickness 50.8 μm until they burst. The average burst pressure measured was 39.2 kPa with a standard deviation of 1.1 kPa. Using the hoop stress equation given as:

$$P_{burst} = \sigma_{yield} \left(\frac{t}{R} \right), \tag{4}$$

the material yield stress $\sigma_{yield} = 1.23e4$ kPa can be determined, and leads to $P_{burst} = 61.3$ kPa for our simulations. As

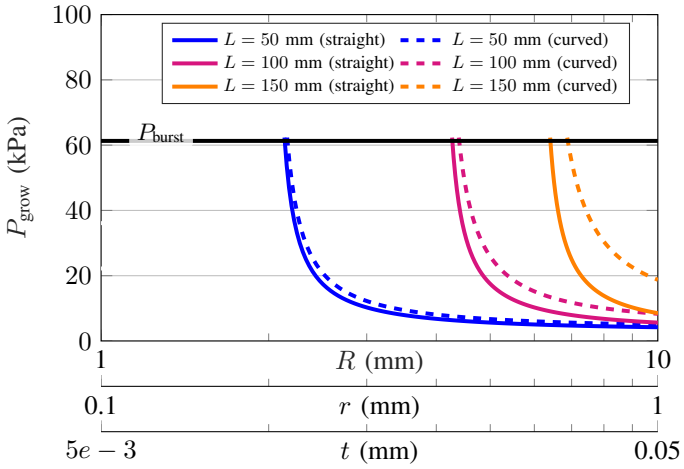

Fig. 3. The model shows that for vine robots with working channels, the growth pressure increases as scale decreases. Shorter vine robots have lower growth pressures, and can thus be scaled smaller before reaching the burst pressure. Straight vine robots (solid lines) require less pressure to grow than curved ones (dotted lines, radius of curvature = 12 mm). Scaling is isometric in the cross section, with working channel radius, main body radius, and material thickness scaling together.

visible in Fig. 3, the pressure required to grow a certain length increases as the vine robot is scaled down, and longer lengths cannot be obtained with small vine robots. Finally, the results also show a pressure increase when growing for a given length in curved paths compared to straight paths. Further analysis is provided in Appendix B, and shows the growth limits of vine robots with no working channel as a comparison.

To summarize, our analysis shows that the pressure required to grow scaled-down vine robots with a working channel increases along straight paths, and further increases along curved paths, which can significantly impair their practical use. We showed that this increase in required pressure is primarily due to the internal friction introduced by the working channel, as well as the capstan friction of the tail in curved paths. To overcome these limitations, we propose in the next section the concept of storing scrunched material at the tip of the vine robot.

III. Proposition of New Vine Robot Concept

In this section, we propose a concept that essentially eliminates the internal friction between the tail and working channel to overcome the growth limits of previous designs with working channels in straight and curved paths. Critically, the concept provides a working channel that enables access to the very tip of the vine robot at any time during continuous growth. Our proposed concept relies on the principal of material scrunching. While the concept of material scrunching has been proposed for vine growing robots [19], [20], the tail was scrunched at intermediate locations along the body [20] or at the base of the vine robot, as a replacement to spools typically used to store the tail material. The goal of the latter approach was to ease the passage of camera wires through the tail. In our work, we propose to decrease and suppress the effective contact length between the vine robot tail and the working channel or between the vine robot tail and its body by scrunching the tail at the tip of the vine robot. We propose both an everting, scrunched design and a non-everting, scrunched design in the following sections.

A. Everting Scrunched Design

Our analysis in Section II showed that the contact area between the vine robot tail and working channel, as well as contacts between the tail and its body, both lead to growth limits. To overcome these limitations, we propose to scrunch the tail at the very tip of the vine robot, around the working channel (Fig. 4). This design allows us to lower the effective contact area between the vine robot tail and both the working channel and vine robot body. In order to prevent friction between the scrunched tail and the vine robot body, a thin constraining layer, with a radius R_c, smaller than that of the vine robot body R, is placed around the scrunched material. In this work, we assume that the length of scrunched material is sufficiently short with respect to the local radius of curvature of the path, such that the scrunched material does not need to bend, and such that there is negligible friction between the constraining layer and the vine body (see Fig. 4). We also assume that unscrunching the material does not require any

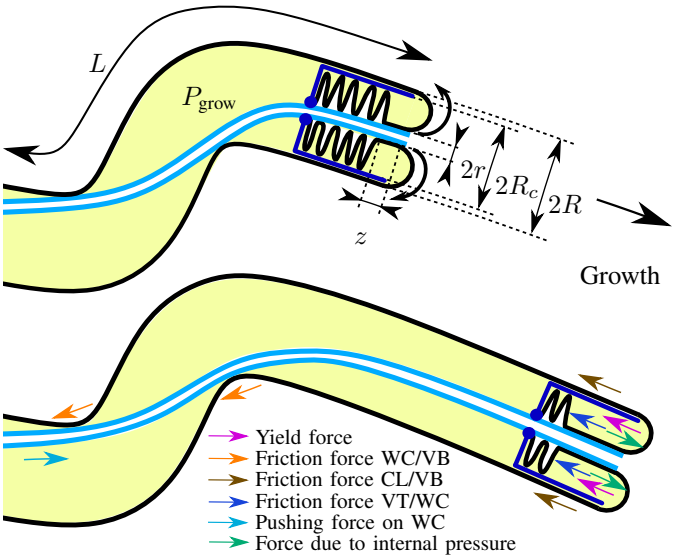

Fig. 4. Illustration of our proposed everting scrunched vine growing robot with a working channel at two different growth stages, with its design parameters represented in the top configuration and free body diagram representing the forces in the bottom configuration.

force, i.e. that the layers of material are not blocked due to the material being tightly packed.

Next, we modify Eq. (2) to understand the growth capabilities of the proposed everting scrunched design. In order for the vine robot to grow, the pushing force exerted by the internal pressure must overcome the yield force and friction forces between the deploying tail and the tip of the working channel. This leads to a first growth condition, as shown in Eq. (5), *top*. Since the internal pressure can cause the scrunched material to deploy past the working channel tip, the working channel must be translated at its base in order to stay aligned with the vine robot tip. We note that pushing the working channel is not used to aid in the growth of the robot. The friction force $\mu_{\text{VT/WC}} P_{grow} 2\pi r z$ between the working channel and the vine tail aids in the translation of the working channel, which must overcome the friction forces between the working channel and the vine body ($F_{\text{WC/VB}}$) and between the constraining layer and the vine body ($F_{\text{CL/VB}}$). This leads to a second growth condition, as shown in Eq. (5), *bottom*. These two conditions of deployment are expressed by the following system:

$$\begin{cases} \frac{1}{2} P_{grow} \pi (R^2 - r^2) = \frac{1}{2} F_y + \mu_{\text{VT/WC}} P_{grow} 2\pi r z \\ F_{\text{Push}} = F_{\text{WC/VB}} + F_{\text{CL/VB}} - \mu_{\text{VT/WC}} P_{grow} 2\pi r z \end{cases}, \quad (5)$$

where z is the contact length between the deploying tail material and the working channel. Assuming that the short scrunched length results in negligible friction in curved paths, our proposed design does not require a pressure increase for growth in curved paths. This is an important benefit, as maintaining a growth pressure well below burst pressure, even in curved paths, is critical for practical applications.

We assume that the pushing force provided at the base of the working channel is large enough to compensate for the friction forces between the working channel and the vine robot body. We therefore focus on the first equation of the system

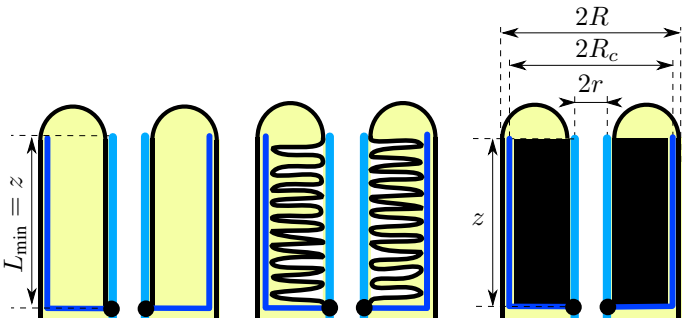

Fig. 5. Representation of the scrunched material with (a) the highest compression ratio $\epsilon = \epsilon_{\text{min}}$, (b) an intermediate compression ratio and (c) the lowest compression ratio ϵ_{max}.

in Eq. (5). The effective friction length between the vine robot tail and the working channel is z, compared to L in previous designs. Since the material is scrunched, we have $z \leq L$, and the difference between them depends on how much the material is scrunched.

It is convenient to convert the length of scrunched material at the tip, z, to a deployed length, L, for the vine robot. The material is scrunched between two cylinders of radius R_c and r and length z (see Fig. 5c), resulting in a volume of $\pi(R_c^2 - r^2)z$ where the scrunched material can be stored. The volume of material that is stored inside can be expressed as the material cross-section, $2\pi Rt$, times its length, L. We assume that the extent to which the scrunched material can be compressed will vary, and we define a compression ratio ϵ as the volume occupied by the vine material over the available volume:

$$\epsilon = \frac{2\pi RtL}{\pi(R_c^2 - r^2)z}. \quad (6)$$

There must be at least one layer of material inside the material storage area, as shown in Fig. 5a. Therefore, the minimum length of material that can be stored, and thus the minimum growth length, is $L_{\text{min}} = z$. This case corresponds to the standard design, when only a layer of material is present along the working channel, without scrunches. This leads to a minimum scrunching ratio $\epsilon_{\text{min}} = \frac{2Rt}{R_c^2 - r^2}$. In its most compact form, we assume that the volume for material storage is full of material, such that we have $\epsilon_{\text{max}} = 1$, as illustrated in Fig. 5c. This leads to $L_{\text{max}} = \frac{(R_c^2 - r^2)z}{2Rt}$, which is the maximum length of material which can be stored, and thus the maximum growth length. An illustration of an intermediate case with $\epsilon_{\text{min}} \leq \epsilon \leq \epsilon_{\text{max}}$ is shown in Fig. 5b.

Given that the minimum growth length of our everting scrunched design, $L_{\text{min}} = z$, is equal to the growth length of the standard design, the gain, G, in growth length between the designs can be expressed as $\frac{L}{z}$ using Eq. (6) as:

$$G = \epsilon \left(\frac{R_c^2 - r^2}{2Rt} \right). \quad (7)$$

Using the first equation in Eq. (5) and Eq. (6), and assuming LDPE for the vine material, the growth pressure of our everting scrunched vine robot is then expressed as:

$$P_{\text{grow}} = \frac{kt^2}{\pi(R^2 - r^2) - \mu_{\text{VT/WC}} 4\pi r \left(\frac{2\pi RtL}{\pi(R_c^2 - r^2)\epsilon} \right)}. \quad (8)$$

For $\alpha \in [0, 1]$, we can see that $P_{grow}(\alpha R, \alpha r, \alpha t) \geq P_{grow}(R, r, t)$, meaning that a scaled-down everting scrunched vine robot requires higher pressure to grow a given length. The gain in terms of growth length given by Eq. (7) greatly reduces the growth pressure at any given length and scale compared to non-scrunched designs. Interestingly, we can also see that when α tends to infinity, P_{grow} converges to $\frac{kt^2}{\pi(R^2-r^2)}$, which does not depend on ϵ. This means that, as the scale increases, vines that are scaled relative to one another will grow at the same pressure, regardless of their compression ratio. These elements are key for practical use, as illustrated in the following example.

We consider the vine robot from Section II-B with $r/R = 0.1$, $\mu_{\text{VT/WC}} = 0.1$, $t/R = 0.005$, $\mu_{\text{VT/VB}_c} = 0.22$, $C = 0.08$, $L = 150$ mm and a burst pressure of 61.3 kPa in the case of LDPE. For our simulations, we assume $R_c \approx R$. Using Eq. (8), we plot the values of the pressure required to grow as a function of R as vine robots are scaled down. We note that the uncertainty for various design parameters can be propagated to perform sensitivity analysis on the growth pressure if desired. As visible in Fig. 6, the standard design, which in the case of straight paths is equivalent to the scrunched everting design with $\epsilon = \epsilon_{\text{min}}$, cannot grow for 150 mm for $R \leq 6$ mm. We can also see that for the standard design, the dependency on path curvature further increases the growth pressure and limits the growth length. In contrast, for a given radius R, the growth pressure of our proposed everting scrunched design decreases when ϵ increases. Thus, our everting scrunched vine robot enables growth at lower pressures, and the growth pressure does not depend on the path geometry. We also note that, as predicted by our model, the growth pressures all converge to the same value as the scale increases. Finally, the growth pressure curves do intersect with the burst pressure line, meaning that below a certain radius, these vine robots cannot grow for a length of $L = 150$ mm. Indeed, vine robots with $\epsilon = 0.5$ cannot grow for 150 mm if $R \leq 0.1$ mm, while vine robots with $\epsilon = 0.75$ or 1.00 can. Overall, our everting scrunched vine robot enables growth of robots that would not grow without scrunches.

We now consider the practical case where application requirements constrain the radius of the working channel, and a robot body as small as possible is desired. Thus, we assess how scaling the vine robot body and material thickness affect growth pressure, while the working channel radius remains constant. We consider the same robot as previously, with the parameters $\mu_{\text{VT/WC}} = 0.1$, $t/R = 0.005$, $\mu_{\text{VT/VB}_c} = 0.1$, $L = 150$ mm, and a burst pressure of 61.3 kPa in the case of LDPE, and then scale its body and material thickness, with $r = 1$ mm. As visible in Fig. 7, the pressure required to grow increases significantly as the vine robot radius approaches the working channel radius, which limits the growth length of these robots.

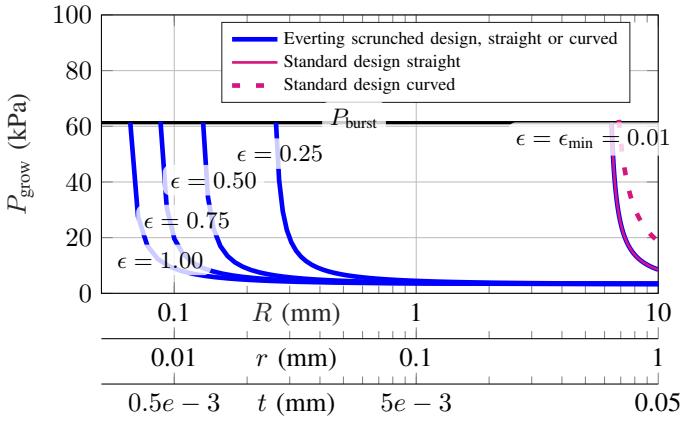

Fig. 6. Pressure required to grow a 150 mm vine robot as it is scaled down, for the standard design and our everting scrunched design with different compression ratios (ϵ). While the standard design cannot grow for 150 mm for $R \leq 6$ mm, the scrunched everting design succeeds, particularly when the compression ratio is high.

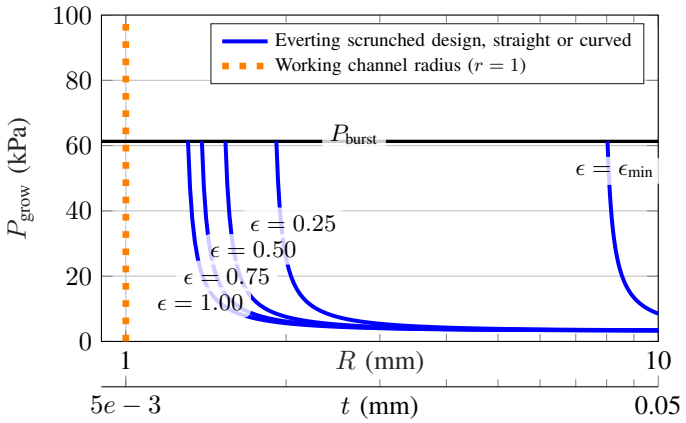

Fig. 7. Pressure required to grow as a function of R as the body and material thickness of an everting scrunched vine robot are scaled, while the working channel radius remains constant ($r = 1$ mm). The graph shows that under these scaling conditions, the pressure required to grow increases as the vine robots are scaled down, and that working limits are reached with our proposed everting scrunched design when the difference between R and r becomes too small.

B. Non-Everting Scrunched Design

The previous design with material scrunching and eversion significantly decreases the pressure to grow a given length compared to the standard design in Section II. However, the friction force between the tail and the working channel leads to an increase in growth pressure and decrease in growth length limits, particularly when the difference between the vine robot radius (R) and working channel radius (r) becomes small. In addition, the presence of the yield force, F_y, leads to an offset in the pressure required to grow, and can prevent the vine robot from growing if $P_{\text{burst}} < P_{\text{grow}}$. This condition occurs when R tends to r, in which case P_{grow} tends to infinity, while P_{burst} remains constant (see Eq. (4) and Eq. (8)).

In order to overcome this limitation, we present a new vine robot design where the material is attached to the tip of the working channel and is scrunched around it at its distal end, without eversion, as illustrated in Fig. 8. The vine material unscrunches from the base of the scrunched material, enabling

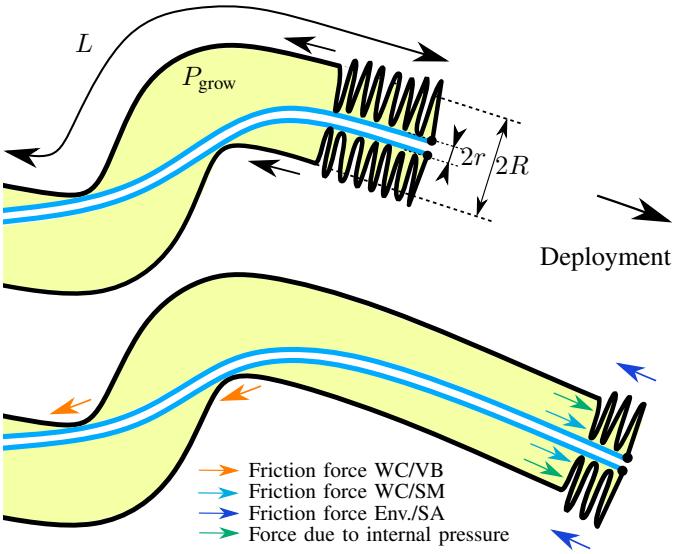

Fig. 8. Illustration of our proposed non-everting scrunched vine robot with a working channel at two different deployment stages. The design parameters are represented in the top configuration and the free-body diagram representing the forces are shown in the bottom configuration.

deployment of the robot. We again assume that unscrunching the material does not require any force, i.e. that the material layers are not blocked due to the material being tightly packed. This design enables the elimination of the yield force and removes the friction force between the vine robot tail and the working channel, which was the main limiting factor of our previous everting scrunched design. We note that these benefits come with a tradeoff, which is that in our non-everting design, the scrunched material at the tip undergoes rigid-body translation with respect to the environment (see Fig. 8). While this may not be as ideal as the everting design, we show below that the net resistance to growing can be reduced with the non-everting design. Further, root tips actually grow in this manner with a small section translating forward at the tip, as was noted by work that uses tip-based additive manufacturing with a similar translating section [21].

Next, we modify the analysis from Section II to understand the deployment limits of the proposed non-everting scrunched design. In this design, the working channel displacement is directly related to the vine robot deployment, since it is attached at the vine robot tip. Thus, the condition of deployment is expressed in a single equation, given as:

$$\frac{1}{2}P_{grow}\pi(R^2 - r^2) + F_{\text{WC/SM}} = F_{\text{WC/VB}} + F_{\text{Env./SA}}, \quad (9)$$

where $F_{\text{WC/SM}}$ is the force transmitted by the working channel to the scrunched material, $F_{\text{WC/VB}}$ is the friction force between the working channel and the vine body, and $F_{\text{Env./SA}}$ is the friction force between the environment and the scrunched material (shown in blue in Fig. 8). We note that in this design, since the working channel is attached to the tip of the vine material, $F_{\text{WC/SM}}$ can exceed $F_{\text{WC/VB}} + F_{\text{Env./SA}}$ in magnitude and lead to deployment without significant internal pressure. The friction force with the environment can be expressed as:

$$F_{\text{Env./SA}} = \mu_{\text{Env./SA}} F^{NS}_{\text{Env./SA}} A_{\text{SA}}, \quad (10)$$

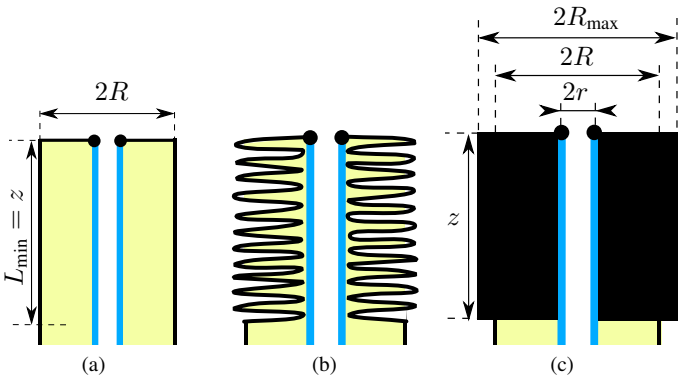

Fig. 9. Representation of the scrunched material with (a) the lowest compression ratio $\epsilon = \epsilon_{\min}$, (b) an intermediate compression ratio, and (c) the highest compression ratio $\epsilon = 1$.

where $\mu_{\text{Env./SA}}$ is the friction coefficient between the environment and the scrunched area, $F^{NS}_{\text{Env./SA}}$ is the normal surface force between them, and A_{SA} is the surface of the scrunched area. It is possible to express A_{SA} as a function of the vine robot radius (R), length of material scrunched (L), material thickness (t), working channel radius (r), and compression ratio (ϵ). Representations of the scrunched material for $\epsilon = \epsilon_{\min}$ (i.e. no scrunching), $\epsilon = 1$ (most compact), and an intermediate case are shown in Fig. 9. In its most compact form, the scrunched material occupies a maximum radius $R_{\max}$, illustrated in Fig. 10a, due to the arrangement of the material around the working channel. In order to estimate the radius $R_{\max}$, the angle θ, represented in Fig. 10b, must first be identified. We consider a point $B = \begin{bmatrix} r\cos\theta & r\sin\theta \end{bmatrix}^\intercal$ on the circle. The intersection between the tangent of the circle at point B and the vertical axis that intersects with O is $C = \begin{bmatrix} 0 & \frac{r}{\sin\theta} \end{bmatrix}^\intercal$. Knowing that the length of the arc from A to C, $\overset{\frown}{AC}$, is a quarter of the vine robot body perimeter, and knowing the location of points B and C, we can write $\overset{\frown}{AC} = \overset{\frown}{AB} + \overset{\frown}{BC}$ as:

$$\frac{2\pi R}{4} = r\left(\theta + \sqrt{\frac{1}{\sin^2\theta} - 1}\right). \quad (11)$$

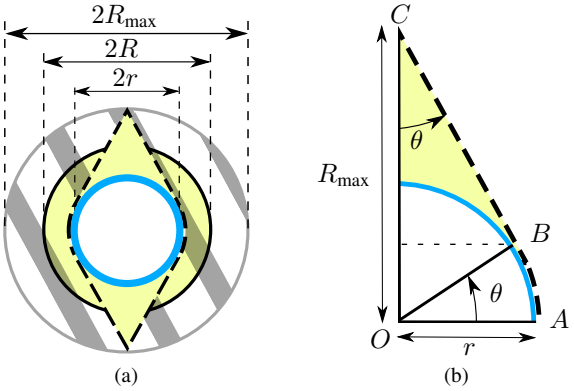

Fig. 10. (a) Front view in the deployment direction of the vine robot represented in Fig. 8, in the case of scrunched material with the highest compression ratio ($\epsilon = 1$), and (b) close up view which shows additional design parameters for modeling purposes.

Solving Eq. (11) for θ, the maximum scrunched radius, R_{max}, can then be calculated as:

$$R_{\text{max}} = \frac{r}{\cos\theta}\sqrt{\frac{1}{\sin^2\theta} - 1}. \tag{12}$$

It is convenient to convert the length of scrunched material at the tip, z, to a deployed length, L, for the vine robot. Similar to the scrunched everting design, the compression ratio ϵ is computed as the ratio of volume occupied by the vine robot material over the available volume as:

$$\epsilon = \frac{2\pi RtL}{\pi(R_{\text{max}}^2 - r^2)z}. \tag{13}$$

The minimum length of material that can be stored corresponds to a single layer being present in the scrunching area. This corresponds to $L_{\text{min}} = z$, as represented in Fig. 9a, leading to a minimum scrunching ratio $\epsilon_{\text{min}} = \frac{2Rt}{R_{\text{max}}^2 - r^2}$. In this case, the surface of the scrunched area is $A_{\text{SA}} = A_{\text{SA,max}} = 2\pi RL$. In its most compact format, the scrunching area is full of material and $\epsilon = 1$, resulting in $A_{\text{SA}} = A_{\text{SA,min}} = \frac{4\pi R_{\text{max}} RtL}{R_{\text{max}}^2 - r^2}$. It is interesting to observe that, in Eq. (13) as z decreases to $\frac{L}{2^n}$ with $n \in \mathbb{N}$, ϵ increases using the law $\epsilon = \epsilon_{\text{min}} 2^n$.

In order to express A_{SA}, we assume that it follows a similar trend, such that as z decreases to $\frac{L}{2^n}$ with $n \in \mathbb{N}$, A_{SA} decreases from its initial value by a factor of 2^n, and is written as $A_{\text{SA}} = A_{\text{SA,max}} 2^{-n} = 2\pi RL \times 2^{-n}$. This assumption holds if the radius of the scrunched area remains approximately constant and equal to R while its length decreases. Although the radius actually varies between R and R_{max}, because R_{max} cannot be greater than $\frac{\pi R}{2} \approx 1.57R$ (for the case when $r = 0$), this assumption is reasonable. Since we have $\epsilon = \epsilon_{\text{min}} 2^n$, A_{SA} can be expressed as a function of ϵ:

$$A_{\text{SA}} = 2\pi(L - L_{\text{dep}})R \times 2^{\left(-\frac{\log\left(\frac{\epsilon}{\epsilon_{\text{min}}}\right)}{\log(2)}\right)} \tag{14}$$

where L_{dep} is the length of material that has already been deployed. As visible in Eq. (14), the surface of scrunched material is maximal at the beginning of the deployment when $L_{\text{dep}} = 0$, and equals zero at the end of the deployment, where $L_{\text{dep}} = L$. Thus, the potential surface of friction between the vine robot and the environment decreases as the robot deploys. Since the non-everting scrunched design can be deployed at lower pressure by pushing the working channel (see Eq. (9)), we focus our simulations on A_{SA}, which impacts the friction force between the vine robot and the environment.

To investigate how A_{SA} varies as a vine robot is scaled, we consider a vine robot made of LDPE with $r/R = 0.5$, $t/R = 0.017$, $L = 150$ mm. We compute the scrunched area, A_{SA}, when the vine robot is fully retracted, i.e. $L_{\text{dep}} = 0$. In Eq. (11), it is visible that if the ratio r/R is fixed, the angle θ remains constant as vine robots are scaled down. In Eq. (12), we can see that R_{max} then becomes a linear function of r, which leads to A_{SA} varying linearly as a function of the scaling ratio. This relationship is illustrated in Fig. 11.

We now consider the practical case where application requirements constrain the radius of the working channel, and

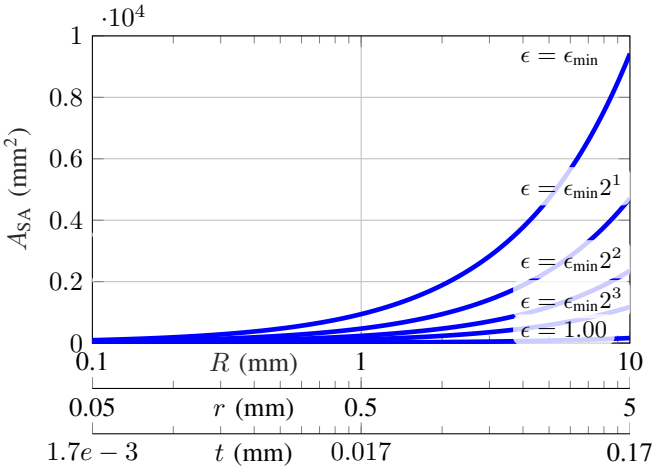

Fig. 11. Variations of scrunched material area as a function of R as the vine robot is scaled down, for different compression ratios ϵ. For all compression ratios, the area of scrunched material decreases as the non-everting scrunched vine robot is scaled down, and as the compression ratio increases.

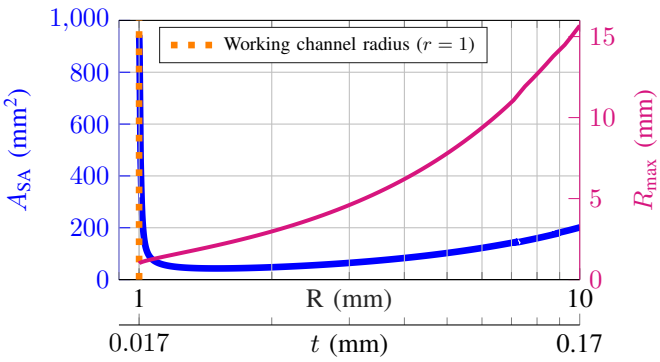

Fig. 12. Variations of R_{max} and A_{SA} when the vine robot body and material thickness are scaled, while the working channel radius remains constant ($r = 1$ mm), for a compression ratio of $\epsilon = 1$. For $R > 1.2$ mm, the radius of the scrunched material, R_{max}, increases, while the scrunched area, A_{SA}, remains relatively constant, showing that the radius of scrunched material can be controlled to be small without increasing its exposed surface by selecting a proper scaling ratio.

a robot body as small as possible is desired. Thus, we assess how scaling the vine robot body and material thickness affect the geometry of the scrunched area, for a compression ratio of $\epsilon = 1$, which is the most favorable to lower the surface of contact with the environment. The vine robot material is LDPE with $t/R = 0.017$, $L = 150$ mm, as in the previous study, and we set $r = 1$ mm. The simulation results are visible in Fig. 12. They show that as R is scaled down towards r, R_{max} continuously decreases. A_{SA} also decreases slightly initially, but experiences a sharp increase for $R < 1.2$ mm. Indeed for $R < 1.2$ mm, there is a clear trade-off between minimizing the potential surface of friction and maintaining a small overall diameter. However, for $R > 1.2$ mm, the scrunched area, A_{SA}, only increases slightly, even as the radius of the scrunched material, R_{max} increases. This shows that R_{max} does not need to be constrained to be small to obtain small values of A_{SA}, by selecting the proper scaling ratio.

C. Comparison of New Scrunched Designs

We next conduct a direct comparison between the non-everting and the everting scrunched designs as the scale decreases, and also compare them to the standard design. Following the same hypothesis as our everting scrunched design, we assume that enough force is provided at the base of the working channel to overcome the friction force between the working channel and the vine robot body, such that Eq. (9) simplifies to $\frac{1}{2}P_{grow}\pi(R^2 - r^2) = F_{\text{Env./SA}}$. We consider a vine with parameters $r/R = 0.5$, $\mu_{\text{VT/WC}} = 0.1$, $t/R = 0.017$, $L = 150$ mm, a burst pressure of 205 kPa, and scrunching ratios of 0.5 and 1.0. We assume a uniform normal surface force applied by the environment onto the non-everting scrunched vine. Here the normal surface force considered is $F^{NS}_{\text{Env./SA}} = 2$ N/m^2, with a friction coefficient $\mu_{\text{Env./SA}} = 0.2$. Under the assumption of uniform normal surface force, $F_{\text{Env./SA}}$ is maximum at the very beginning of the deployment, and is used in our simulation to compute P_{grow}.

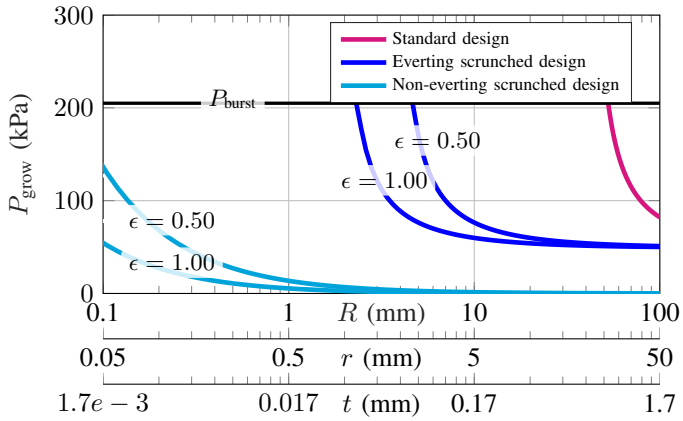

Fig. 13. Comparison of the pressure required to grow a 150 mm vine robot as it is scaled down, for the standard design, the everting scrunched design, and the non-everting scrunched design. While the standard design cannot grow for 150 mm for $R \leq 50$ mm, our proposed scrunched designs can. Also, while the everting scrunched design cannot grow for $R \leq 2$ mm, the non-everting scrunched design succeeds depending on the friction force with the environment, particularly when the compression ratio is high.

As visible in Fig. 13 , the standard design can grow for 150 mm with a radius as small as 50 mm, and cannot grow at a smaller scale for that length. In contrast, the everting scrunched vine can grow for 150 mm at a radius close to 2.0 mm for a compression ratio $\epsilon = 1$, with a pressure close to the burst pressure. The non-everting scrunched vine can grow at an even smaller scale, depending on the friction force with the environment.

IV. Experimental Evaluations

In this section, we conduct experimental evaluations in order to validate the models and overall performance of our new vine robot designs.

A. Everting Scrunched Design

1) Model Validation: In order to evaluate the accuracy of the model in Eq. (8), we fabricate and test three vine robots, scaled relative to one another. We also vary their compression ratios, and measure the pressure required to grow a specified length.

a) Model Parameters: To obtain parameters for three isometrically scaled vine robots, we start by selecting off-the-shelf materials with different thicknesses, t. The ratios between the material thicknesses determines the scaling ratios, which are used to determine the other geometric parameters, R and r. Here we select LDPE with material thicknesses of 50 μm (Everting design 1), 100 μm (Everting design 2) and 150 μm (Everting design 3). Based on the resulting scaling ratios, we then set R to be 3.5, 7.0 and 10.5 mm, and r to be 0.5, 1 and 1.5 mm, respectively. PTFE tubes are selected for the working channels in order to have low values of $\mu_{\text{VT/WC}}$. Friction tests between these two material lead to an avergage value of $\mu_{\text{VT/WC}} = 0.16$. Using Eq. (4) with $\sigma_{yield} = 1.23e4$ kPa, the theoretical burst pressure of our robots is found to be 178 kPa (larger than the value of 61.3 kPa previously considered since the ratio t/R is different), and sets the upper limit for our growth pressure.

b) Fabrication: We fabricated our everting scrunched vine prototypes using the steps described below. They are illustrated in Fig. 14 and are visible in the provided video.

(i) The working channel is first inserted through the main channel of a fabricated Y-connector, and an air line is connected to its side channel. Clearance between the main channel of the Y-connector and the working channel enables air to travel around the working channel to pressurize the vine robot, and an air-seal prevents leakage at the base of the Y-connector.
(ii) The base of the vine material, which constitutes its tail, is attached and air-sealed around the working channel.
(iii) A constraining tube is assembled around the tail of the vine robot and working channel.
(iv) The tail is scrunched between the working channel and the constraining tube. A tube that fits between the working channel and the constraining tube can be used to press on the scrunched tail and increase its compression ratio.
(v) The tip of the scrunched material is everted over the constraining tube. It is attached and sealed to the tip of the Y-connector.

c) Experimental results: First, the yield force, F_y, was identified following the method in Appendix A. The growth pressure was measured three times for each design. As expected for isometrically scaled designs, the growth pressures were found to be similar, with pressures of 29.5 ± 0.21, 25.6 ± 0.23 and 27.7 ± 0.40 kPa for the everting designs 1, 2 and 3, respectively. This leads to yield forces of 1.13 ± 0.01, 3.94 ± 0.04 and 9.59 ± 0.14 N for the three designs, respectively, which confirms the quadratic trend $F_y = kt^2$ previously identified (see Appendix A).

The three vine robots were then fabricated and assembled with three different compression ratios each ($\epsilon = 0.1$, $\epsilon = 0.2$ and $\epsilon = 0.3$) and grown three times for a length of 100 mm. These scrunching ratios correspond to lengths $z = 29.2$, 14.6 and 9.7 mm, respectively. In this work, we performed human-in-the-loop deployment with visual feedback to keep

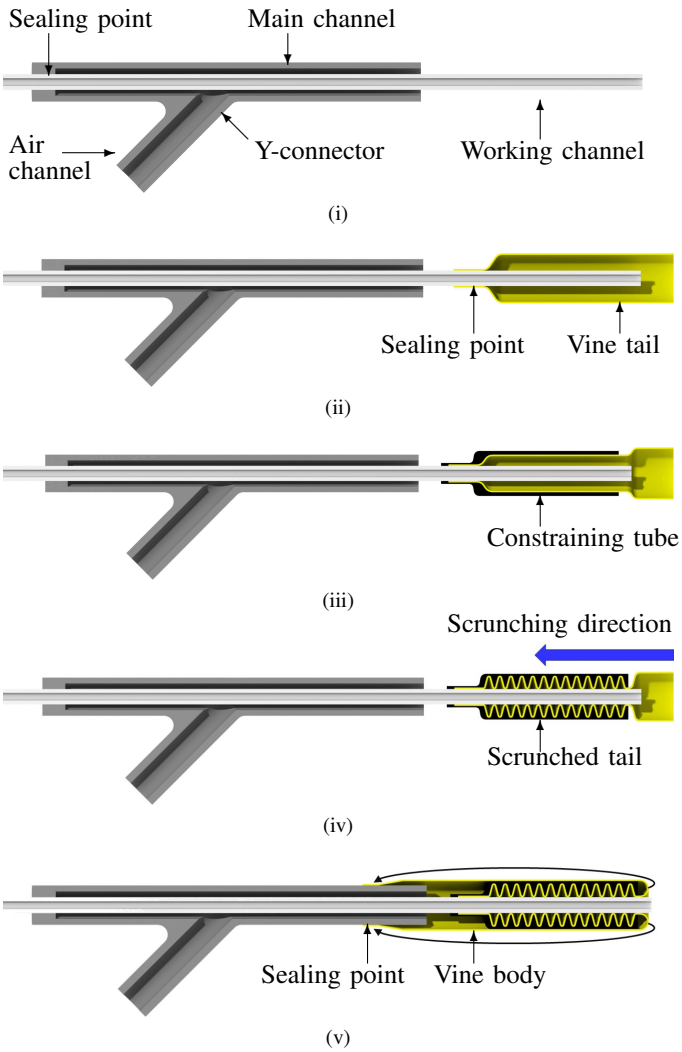

Fig. 14. Fabrication steps for our proposed everting vine robot prototype include (i) insertion of the working channel inside the Y-connector, (ii) attachment of the vine robot tail to the working channel, (iii) attachment of the constraining tube over the vine robot tail, (iv) scrunching of the tail, and (v) eversion and attachment of the vine robot onto the Y-connector to form the vine robot body.

the working channel at the tip, with the user manually controlling both the internal vine pressure and the working channel displacement. The average pressure required to obtain this length of growth was measured and is shown in Fig. 15, along with the expected pressures required to grow 100 mm as a function of R based on the model. Larger errors are observed for the smallest design (everting design 1) with the smallest compression ratio $\epsilon = 0.1$. These larger errors could be explained by modeling inaccuracies of the surface of contact between the vine tail and the working channel at such a small scale. However, overall, our experimental results are in general agreement with our simulations, validating the scaling performance of our scrunched everting design.

2) Performance Validation: In order to validate the performance of the everting scrunched design, we fabricated and tested a prototype in both a straight and curved path and compared its performance to that of the standard design. Dimensions were selected based on requirements for

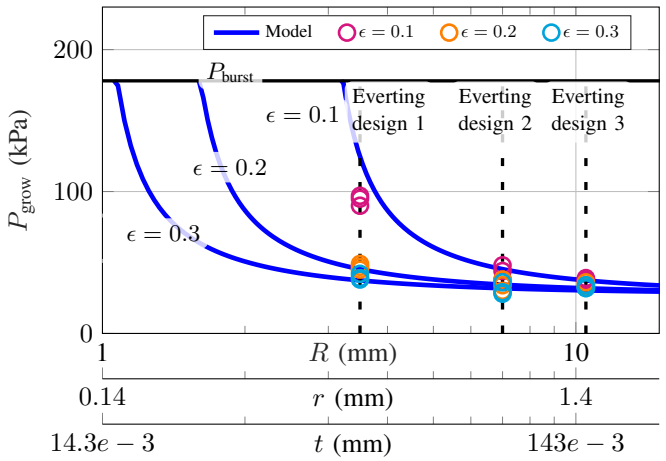

Fig. 15. Experimental results which show the pressure required to grow three vine robots scaled relative to one another (Everting design 1 of radius 3.5 mm, Everting design 2 of radius 7.0 mm, Everting design 3 of radius 10.5 mm), for a deployed length of 100 mm, for compression ratios $\epsilon = 0.1$, 0.2 and 0.3.

colonoscopy—a clinical application for which these robots could help to improve safety and outcomes. A vine robot with a diameter of 12.9 mm and a length of 1500 mm was fabricated using Dyneema 0.34—a composite material with fiber reinforcement, selected for its high burst pressure to material thickness ratio. It has a measured average thickness of 0.021 mm. A PTFE working channel with a diameter of 4 mm was used, and a thin tube of diameter 12.2 mm was used as the constraining layer to contain the scrunched material. Lubricant (Super Lube 52004) was added between the PTFE tube and the robot tail. To identify ϵ, we scrunched the vine robot inside the constraining layer and measured this scrunched tail length to be 36 mm. Using Eq. (6), this corresponds to a compression ratio of $\epsilon = 0.34$.

a) Standard Design: We first evaluated the standard vine robot design in order to compare its performance with our model and assess its growth length capabilities. To do so, we built the prototype visible in the first row of Table I. It consisted of the dyneema tube everted around the PTFE working channel, with the tail material loosely stored at the base. The experimental setup consisted of an Arduino

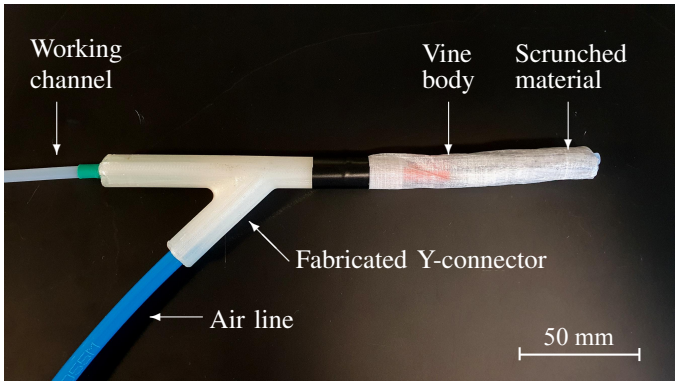

Fig. 16. Photo of the fabricated everting vine robot design with scrunched material and working channel.

Uno controlling a pressure regulator (QBX Series Pressure Regulator, Proportion-Air, Inc., McCordsville IN, USA), and breadboard with switches to manually increment and decrement the pressure by step sizes of 1.7 kPa. The pressure was increased progressively inside the vine so that the stored tail material deployed along the working channel, and the contact length between the tail and the working channel is reported. This length corresponds to the growth length of the standard design. Five trials were performed, and the mean and standard deviation of the growth pressure, P_{grow}, as a function of the contact length L are plotted in the first row of Table I, along with the model from Eq. (2) in the case of a straight path. The experiments are in agreement with the model, and lead to a short deployed length of only 36 mm for a pressure of 55 kPa, which is insufficient for colonoscopy.

b) Everting Scrunched Design - Straight Paths: We then fabricated the everting scrunched vine robot design shown in Fig. 16. Our prototype was grown through a clear plastic tube in order to constrain it to be straight during deployment (see the second row of Table I). A total of five trials were conducted as follows. The vine robot was pressurized in steps, starting from atmospheric pressure, and the growth length of the vine robot was measured for each increment. The experiment was stopped after the vine robot reached a growth length of 1500 mm, which corresponds to the application requirement.

As visible in the graph of Table I, the vine robot started growing for an average pressure of 13.1 kPa. The theoretical growth pressure can be calculated by setting $L = 0$ in Eq. (8), which leads to 12.2 kPa and is in accordance with our experimental observations given the resolution of 1.7 kPa used in our setup. It is visible in the graph that the experimental results match the model, with larger errors for deployed lengths of about 1250 mm. The errors can likely be explained by local variations of the vine robot due to nonuniform fabrication, uneven lubrication of the working channel, and twisting of the scrunched material that leads to increased forces exerted by the scrunched material on the working channel and therefore requires higher pressures to grow. The observed impact of these possible failure modes remained low in our experimental validations. Overall, our fabricated prototype grew for a length of 1500 mm to a pressure of 55 kPa, while the standard design grew for a length of 36 mm at the same pressure. This leads to a gain of 42 in growth length between our scrunched everting design and the standard design, validating our model in Eq. (7), which predicted a gain of $G = 41$, and showing the benefits of our proposed design.

TABLE I

EXPERIMENTAL EVALUATION OF THE EVERTING 12.9 MM VINE ROBOT DESIGN FOR THE TARGETED APPLICATION OF COLONOSCOPY, WITH SCHEME OF THE DESIGNS, EXPERIMENTAL SETUP, AND RESULTS. IN THE FIRST ROW, THE PERFORMANCE OF THE STANDARD DESIGN IS SHOWN, WITH DEPLOYED LENGTHS INSUFFICIENT FOR COLONOSCOPY. IN THE SECOND AND THIRD ROWS, OUR EVERTING SCRUNCHED DESIGN IS EVALUATED ALONG STRAIGHT AND CURVED PATHS, WITH AN INCREASE IN GROWTH LENGTH OF 42 TIMES COMPARED TO THE STANDARD DESIGN.

	Design	Physical setup	Experimental results
Standard design	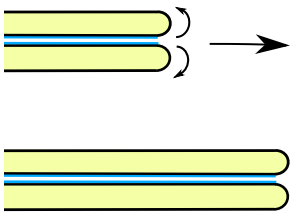	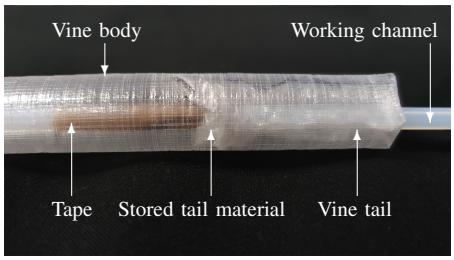	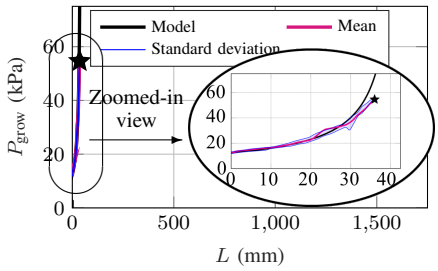
Everting scrunched design	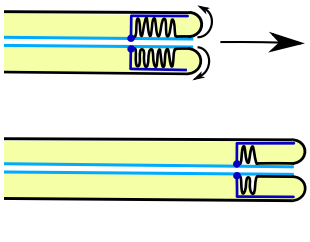	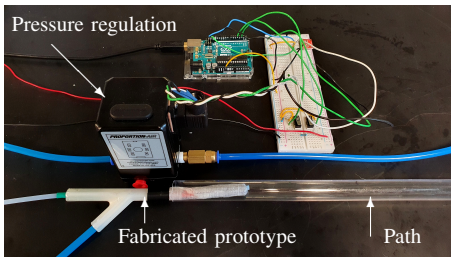	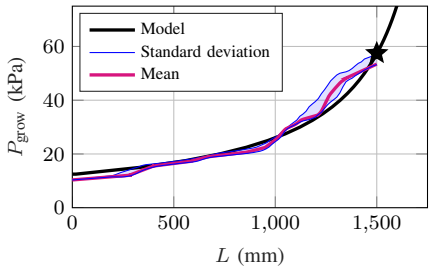
	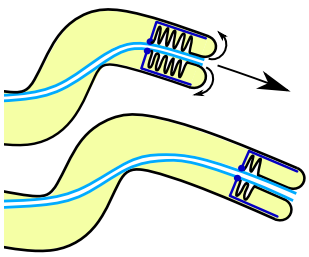	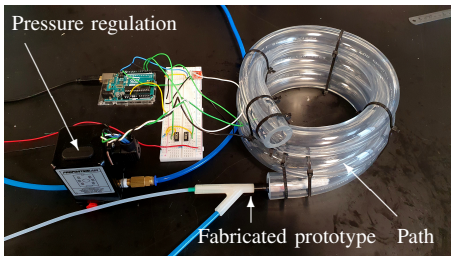	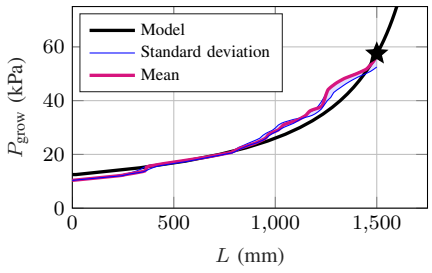

c) Everting Scrunched Design - Curved Path: In order to demonstrate the ability of our design to grow in curved paths, we used the experimental setup shown in the third row of Table I. It consisted of a curved path with a radius of curvature of 80 mm made from a silicone tube. The experimental protocol was the same as for straight paths. The results (see the the third row of Table I) show a good accordance between the experimental results and our model, with larger errors visible for deployed lengths in the neighborhood of 1250 mm. This small discrepancy can again likely be explained by the same factors as in the previous experiment. The results show that the path curvature does not impact the growth pressure of our proposed everting scrunched design.

3) Demonstration: Finally, we demonstrated our everting design in a smaller form-factor, adapted for use in endovascular surgeries. These surgeries increasingly augment or replace traditional open surgical treatment of brain, heart, and vascular diseases, and they require navigation through the vasculature, which often exhibits high curvatures and tortuosity. Vine robots have the potential to help improve safety and efficiency of such procedures [15]. For this demonstration, the vine robot body is made out of Dyneema 0.34 oz, has a diameter of 5.2 mm and a length of 340 mm. The Dyneema is scrunched around a 1.33 mm diameter catheter that serves as the working channel, and it is scrunched inside a PTFE tube (PTFE SLW ETCH .185 ID) from Zeus (Zeus Industrial Products, Inc, Orangeburg, USA) that is 4.7 mm in diameter. The length of scrunched material was measured to be 17 mm. The fabricated prototype is placed at an entry point in the vasculature model as visible in Fig. 17a and grown through the right common carotid artery. A tool (angled 0.36 mm guide wire, TERUMO MEDICAL CORPORATION, NJ, USA) can be used at the tip of the vine robot at any point during the deployment. Three snapshots are taken during deployment, identified as ①, ② and ③ in Fig. 17a, with corresponding close-up pictures visible in Fig. 17b, Fig. 17c, and Fig. 17d, respectively. These still frame images illustrate the deployment capabilities of our design at a smaller scale, while maintaining a tool at the tip.

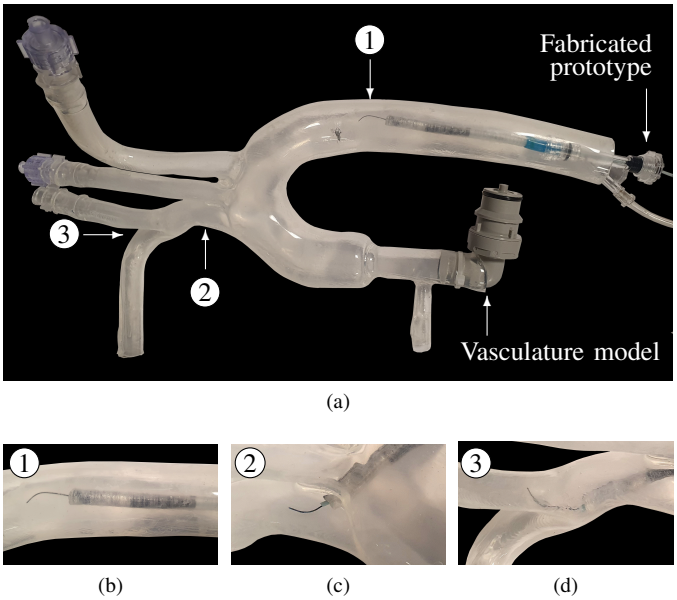

Fig. 17. (a) Photo of the fabricated 5.2 mm diameter everting vine robot design with scrunched material and a 1.33 mm diameter working channel inside a phantom of the aorta. Three deployment stages are labeled, with close-up views visible in (b), (c) and (d).

B. Non-Everting Scrunched Design

1) Model Validation: In order to validate the model for the non-everting scrunched design, we conducted experimental validations on three vine robots of length L = 150 mm, scaled relative to one another. We select LDPE with material thicknesses of 50 μm (Non-everting design 1), 100 μm (Non-everting design 2) and 150 μm (Non-everting design 3). We then set the radius of the vine robots to be 1.5, 3.0 and 4.5 mm, and the radius of the working channel to be 1.0, 2.0 and 3.0 mm for the three designs, respectively. For each design, three compression ratios (ϵ of 0.1, 0.2, and 0.4) were used. These compression ratios were achieved by using Eq. (13) and solving for z, knowing the material thickness t, the vine material radius R, and R_{max} from Eq. (12). After scrunching the vine material for a length z, we then took three measurements of the radius of scrunched material and used the average value to estimate the surface area, assuming a cylindrical shape. This process was performed 3 times for each vine design at each compression ratio. The experimental results are visible in Fig. 18, along with the values predicted by the model in Eq. (14). As visible in this figure, the experimental data follows the model predictions, which is useful for predicting the surface of contact with the environment.

2) Performance Validation: The model for this robot is given by Eq. (14) and shows a linearly decreasing area of scrunched material, or equivalently friction force if the normal force per surface unit is constant during deployment (see Eq. (10)). It has a maximum at the beginning of the deployment, when the surface of scrunched material is maximal, and a minimum of zero at the end of the deployment, when the scrunched material is fully unscrunched. In order to verify this

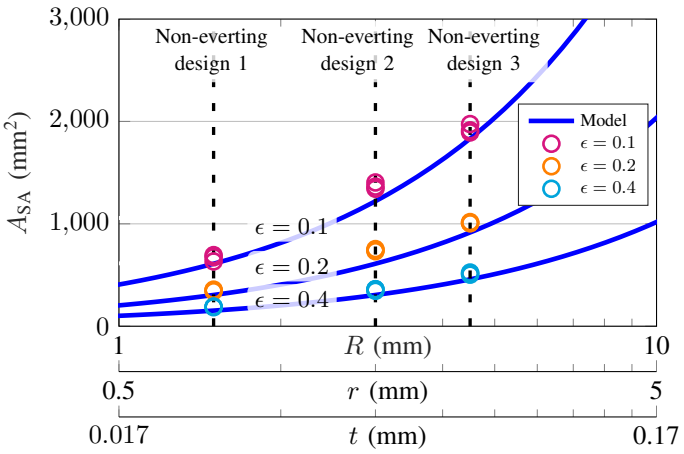

Fig. 18. Experimental results which show the pressure required to deploy three scrunched, non-everting vine robots scaled relative to one another (Non-everting design 1 of radius 1.5 mm, Non-everting design 2 of radius 3.0 mm, Non-everting design 3 of radius 4.5 mm), for a deployed length of 150 mm, for compression ratios $\epsilon = 0.1$, 0.2 and 0.4.

TABLE II
EXPERIMENTAL EVALUATION OF NON-EVERTING VINE ROBOT DESIGN WITH SCHEME OF THE DESIGNS, EXPERIMENTAL SETUP, AND RESULTS.

Design	Physical setup	Experimental results
Non-everting scrunched design	Environment of deployment; Working channel; Air line; Load cell; Linear stage	F (Mean); F (Std Dev); A_{SA} model; F (mN); A_{SA} (mm^2); L (mm)

behavior, we fabricated a physical prototype (Fig. 19) relevant for tasks such as the inspection of industrial parts, for example. It consisted of a vine robot made out of a PTFE tube (PTFE Liner StreamLiner^{TM} VT 0.075") from Zeus (Zeus Industrial Products, Inc, Orangeburg, USA), which was 2.22 mm in diameter. This off-the-shelf tube was selected since manual fabrication of tubes from flat sheets can become challenging at such a small scale. The tube was scrunched in-line with a working channel made out of a Nitinol tube of inner and outer diameters 0.65 and 0.88 mm, respectively. The tail material was scrunched at the very tip of the Nitinol tube, along a length of 16 mm and had an outer diameter of 3.2 mm. The vine robot was then deployed inside a PTFE tube of inner diameter 3.0 mm by pushing its working channel using a linear actuator moving at a constant velocity of 7.1 mm-s^{-1}, and with an internal vine robot pressure of 41.4 kPa. A total of five trials were conducted, and the experimental setup and results are visible Table II. As visible in the graph of Table II, the friction force between the vine robot and the environment decreased during deployment in a nearly linear fashion. The force went from 129.3 mN on average for the first 5 mm of deployment, to 27.1 mN on average for the last 5 mm of deployment. Local non-linearities can be explained by the imperfect cylindrical shape of the scrunched material and by the longitudinal elasticity of the vine robot, which might not have a constant velocity at the tip. This linearly decreasing profile of the friction force is expected based on our model for the area of scrunched material, A_{SA}, which linearly decreases as the robot deploys. The expected values of A_{SA} are overlaid on the plot in Table II, where the initial value was computed using the measured initial length and diameter, and values were then linearly decreased to zero.

3) Demonstration: Inspection tasks are necessary in industrial environments, in order to monitor a system's health, estimate its lifespan, and plan maintenance operations. Such inspection tasks usually require tools, such as cameras for visual inspections, to be inserted inside an environment of interest, through available open channels [22]. In order to represent such tasks, we fabricated a non-everting scrunched vine robot to deploy inside a hole in a wall, which contained electrical wires and water pipes. The fabricated vine robot body had a length of 500 mm, a diameter of 3.0 mm, and a working channel with an outer diameter of 2.0 mm. This prototype, visible in Fig. 20, was deployed for a length of 500 mm by a combination of internal pressure and pushing motion at the base of the working channel. This demonstration highlights the deployment capabilities of this new design in environments where pushing a tool would be difficult because of friction forces along its entire length.

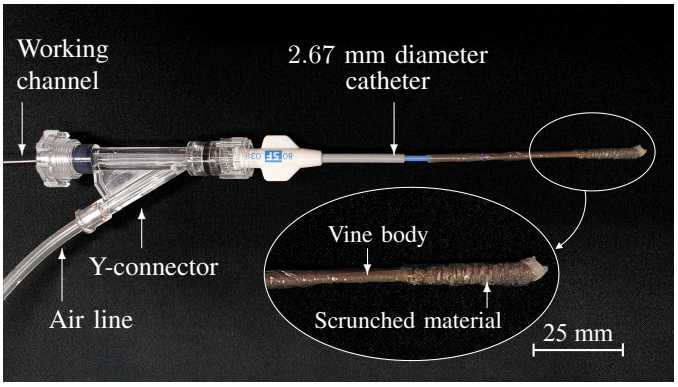

Fig. 19. Photo of the non-everting vine robot design with scrunched material and working channel. The diameter of the vine body is 2.22 mm and the diameter of the scrunched material was measured to be 3.2 mm.

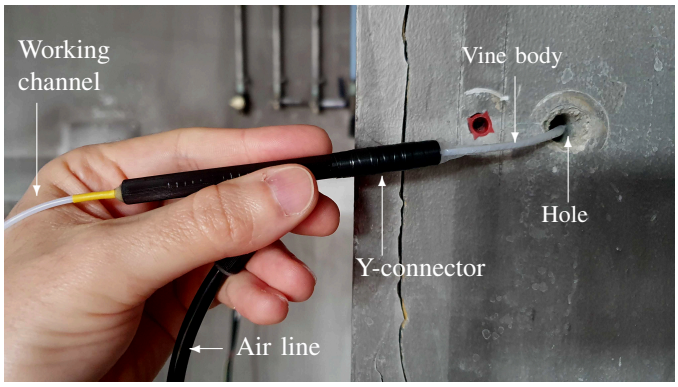

Fig. 20. Photo of our non-everting scrunched robot prototype deploying inside a hole in a wall, with both internal pressure supplied in the vine body and a pushing force applied at the base of the working channel.

V. Conclusion

In this paper, we proposed the concept of scrunching material at the tip of vine robots in order to overcome the growth limits of previous designs with working channels. We presented two new miniaturized vine robot designs that leverage this concept of material scrunching and are able to perform continuous deployment while having a working channel at the tip. Our proposed vine robots overcome limitations of previous designs that were proposed at a larger scale, were not able to grow for significant lengths in the presence of a working channel, or could only perform sequential deployment. We experimentally validated our proposed designs and associated models as the robots are scaled, and evaluated their overall performance. Future work will be focused on the translation of the proposed designs to various applications at a range of scales. To do so, the retraction of such vine robots with working channels will be investigated. In addition, for the scrunched everting design, solutions to prevent the vine material from exceeding the working channel tip, through the use of collars for instance [5], will be implemented. More repeatable methods for scrunching the vine material will also be investigated, particularly for vine robots at smaller scales. Overall, this work enables the creation of vine robots with working channels at scales that were previously unachievable. Because these designs can be made with diameters < 1 cm and allow tool access at all points of deployment during continuous growth, they have the potential for significant impact in applications such as minimally invasive surgery.

Appendix A
Yield Force Model

In previous work, it was found that the yield force of vine robots is independent of its cross-sectional area [16]. We thus assume that it only depends on the material thickness. This relationship is determined through experimental testing. Low-density polyethylene (LDPE) vine robots with varying thicknesses (50.8 μm, 76.2 μm, 101.6 μm, and 152.4 μm) and a diameter of 64 mm were tested. Three vine robots were grown for each thickness, with 10 growth pressure data points collected for each vine robot throughout the deployment. For growth along a straight path with no working channel, Eq. (2) simplifies to $P_{grow} = \frac{F_y}{\pi R^2}$, which was used to compute F_y, and the average values are presented in Fig. 21.

Note that the yield force for LDPE approximately increases with the square of the vine robot wall thickness (fitted model is $F_y = 3.95e8t^{2.0111} \approx kt^2$ with $R^2 = 0.9737$). This relationship between yield force and wall thickness was examined in previous work, however, the study did not test for a large enough range of thicknesses to identify the quadratic trend [23]. Although there is some uncertainty in the measurements, fitted models through points one standard deviation higher and lower than the average points result in exponents of 1.92 and 2.16, respectively, providing a range for expected values of this exponent. In this work, we use 2.0, but the general trends found would not change substantially with slight variations of the exponent.

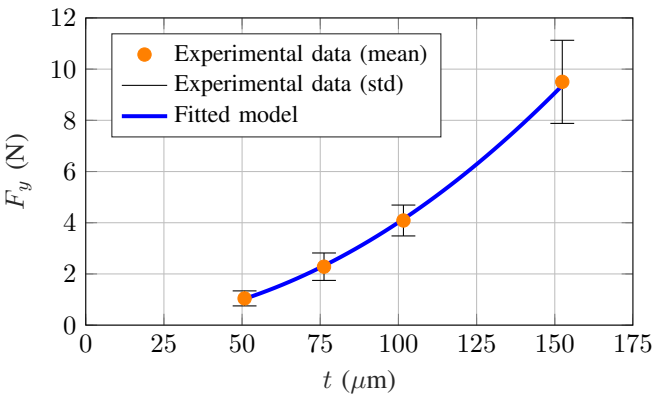

Fig. 21. Results showing the experimental values of the yield force (F_y) as a function of the material thickness (t) for a LDPE vine robot (64 mm in diameter), along with a fitted model.

Appendix B
Growth Limits With no Working Channel

It is useful to compute the growth limits in the case of no working channel in order to better understand the limits imposed by the working channel. Eq. (2) can be modified by setting $r = 0$ and eliminating the friction force in curved regions. The growth pressure of the vine robot can then be written as:

$$P_{grow} = \frac{k}{\pi}\left(\frac{t}{R}\right)^2. \tag{15}$$

The burst pressure can again be derived from the hoop stress equation given by Eq. (4). As the cross section of a vine robot is scaled isometrically (i.e. $t/R =$ constant), growth and burst pressure remain constant. These results imply that if a vine robot can grow at one scale (i.e. the growth pressure is below the burst pressure), it can grow at any scale. This rule is only applicable to vine robots deploying along a straight path without a working channel. Such vine robots unfortunately have very few practical applications.

Acknowledgment

We thank Zeus Industrial Products for providing samples of the PTFE Liners used in our experiments.

References

[1] D. Mishima, T. Aoki, and S. Hirose, "Development of pneumatically controlled expandable arm for search in the environment with tight access," in *Field and Service Robotics*. Springer, 2003, pp. 509–518.

[2] H. Tsukagoshi, N. Arai, I. Kiryu, and A. Kitagawa, "Smooth creeping actuator by tip growth movement aiming for search and rescue operation," in *2011 IEEE international conference on robotics and automation*. IEEE, 2011, pp. 1720–1725.

[3] ——, "Tip growing actuator with the hose-like structure aiming for inspection on narrow terrain." *Int. J. Autom. Technol.*, vol. 5, no. 4, pp. 516–522, 2011.

[4] A. Sadeghi, A. Tonazzini, L. Popova, and B. Mazzolai, "Robotic mechanism for soil penetration inspired by plant root," in *2013 IEEE international conference on robotics and automation*. IEEE, 2013, pp. 3457–3462.

[5] E. W. Hawkes, L. H. Blumenschein, J. D. Greer, and A. M. Okamura, "A soft robot that navigates its environment through growth," *Science Robotics*, vol. 2, no. 8, 2017.

[6] M. M. Coad, L. H. Blumenschein, S. Cutler, J. A. Reyna Zepeda, N. D. Naclerio, H. El-Hussieny, U. Mehmood, J.-H. Ryu, E. W. Hawkes, and A. M. Okamura, "Vine robots: Design, teleoperation, and deployment for navigation and exploration," *IEEE Robotics Automation Magazine*, vol. 27, no. 3, pp. 120–132, 2020.

[7] L. H. Blumenschein, L. T. Gan, J. A. Fan, A. M. Okamura, and E. W. Hawkes, "A tip-extending soft robot enables reconfigurable and deployable antennas," *IEEE Robotics and Automation Letters*, vol. 3, no. 2, pp. 949–956, 2018.

[8] J. Luong, P. Glick, A. Ong, M. S. deVries, S. Sandin, E. W. Hawkes, and M. T. Tolley, "Eversion and retraction of a soft robot towards the exploration of coral reefs," in *2019 2nd IEEE International Conference on Soft Robotics (RoboSoft)*, 2019, pp. 801–807.

[9] N. D. Naclerio, A. Karsai, M. Murray-Cooper, Y. Ozkan-Aydin, E. Aydin, D. I. Goldman, and E. W. Hawkes, "Controlling subterranean forces enables a fast, steerable, burrowing soft robot," *Science Robotics*, vol. 6, no. 55, p. eabe2922, 2021.

[10] S.-G. Jeong, M. M. Coad, L. H. Blumenschein, M. Luo, U. Mehmood, J. H. Kim, A. M. Okamura, and J.-H. Ryu, "A tip mount for transporting sensors and tools using soft growing robots," in *2020 IEEE/RSJ International Conference on Intelligent Robots and Systems (IROS)*. IEEE, 2020, pp. 8781–8788.

[11] F. Stroppa, M. Luo, K. Yoshida, M. M. Coad, L. H. Blumenschein, and A. M. Okamura, "Human interface for teleoperated object manipulation with a soft growing robot," in *2020 IEEE International Conference on Robotics and Automation (ICRA)*. IEEE, 2020, pp. 726–732.

[12] L. H. Blumenschein, M. M. Coad, D. A. Haggerty, A. M. Okamura, and E. W. Hawkes, "Design, modeling, control, and application of everting vine robots," *Frontiers in Robotics and AI*, vol. 7, p. 548266, 2020.

[13] P. Berthet-Rayne, S. M. H. Sadati, G. Petrou, N. Patel, S. Giannarou, D. R. Leff, and C. Bergeles, "Mammobot: A miniature steerable soft growing robot for early breast cancer detection," *IEEE Robotics and Automation Letters*, vol. 6, no. 3, pp. 5056–5063, 2021.

[14] C. Larrea, P. Berthet-Rayne, S. Sadati, D. R. Leff, C. Bergeles, and I. Georgilas, "Growing robotic endoscope for early breast cancer detection: Robot motion control," in *Annual Conference Towards Autonomous Robotic Systems*. Springer, 2021, pp. 391–401.

[15] M. Li, R. Obregon, J. J. Heit, A. Norbash, E. W. Hawkes, and T. K. Morimoto, "Vine catheter for endovascular surgery," *IEEE Transactions on Medical Robotics and Bionics*, vol. 3, no. 2, pp. 384–391, 2021.

[16] L. H. Blumenschein, A. M. Okamura, and E. W. Hawkes, "Modeling of bioinspired apical extension in a soft robot," in *Biomimetic and Biohybrid Systems*. Cham: Springer International Publishing, 2017, pp. 522–531.

[17] P. Green, R. Erickson, and J. Buggy, "Metabolic and physical control of cell elongation rate: in vivo studies in nitella," *Plant Physiology*, vol. 47, no. 3, pp. 423–430, 1971.

[18] D. A. Haggerty, N. D. Naclerio, and E. W. Hawkes, "Characterizing environmental interactions for soft growing robots," in *2019 IEEE/RSJ International Conference on Intelligent Robots and Systems (IROS)*, 2019, pp. 3335–3342.

[19] J.-h. Kim, J. Jang, S.-m. Lee, S.-G. Jeong, Y.-J. Kim, and J.-H. Ryu, "Origami-inspired new material feeding mechanism for soft growing robots to keep the camera stay at the tip by securing its path," *IEEE Robotics and Automation Letters*, vol. 6, no. 3, pp. 4592–4599, 2021.

[20] M. Shike, Z. Fireman, R. Eliakim, O. Segol, A. Sloyer, L. B. Cohen, S. Goldfarb-Albak, and A. Repici, "Sightline colonosight system for a disposable, power-assisted, non-fiber-optic colonoscopy (with video)," *Gastrointestinal Endoscopy*, vol. 68, no. 4, pp. 701–710, 2008.

[21] A. Sadeghi, A. Mondini, and B. Mazzolai, "Toward self-growing soft robots inspired by plant roots and based on additive manufacturing technologies," *Soft Robotics*, vol. 4, no. 3, pp. 211–223, 2017, pMID: 29062628. [Online]. Available: https://doi.org/10.1089/soro.2016.0080

[22] Y. Tian, C. Chen, K. Sagoe-Crentsil, J. Zhang, and W. Duan, "Intelligent robotic systems for structural health monitoring: Applications and future trends," *Automation in Construction*, vol. 139, p. 104273, 2022.

[23] A. Saxena, E. M. Pauli, R. S. Haluck, B. Fell, and J. Moore, "Tubular Locomotion and Positioning Using Tip Eversion for Endoscopy," *Journal of Medical Devices*, vol. 14, no. 2, 03 2020, 021004. [Online]. Available: https://doi.org/10.1115/1.4046433

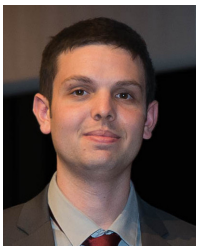

Cédric Girerd received an Engineering degree in Mechatronics from SIGMA Clermont and a Master of Science in Robotics from University Blaise Pascal in Clermont-Ferrand, France, both in 2014. He also received a Ph.D. degree in Robotics from the University of Strasbourg, France, in 2018. He then worked as a Postdoctoral Scholar at the FEMTO-ST Institute in France for one year and at UCSD for three years. Since February 2022, he is a full-time CNRS Researcher in France, and a Visiting Scholar at UCSD. His research focuses on the design and control of continuum and soft robots.

Anna Alvarez received a B.S. from the University of Illinois Urbana Champaign, IL, USA, in mechanical engineering in 2021. Since September 2021, she has been a Ph.D. student at the University of California, Santa Barbara in the Department of Mechanical Engineering. Her focus is on bio-inspired mechanisms, both on the macro and micro scale.

Elliot W. Hawkes received the A.B. degree from Harvard University, Cambridge, MA, USA, in 2009, and the M.S. and Ph.D. degrees from Stanford University, Stanford, CA, USA, in 2012 and 2015, respectively, all in mechanical engineering. He is currently an Assistant Professor with the Department of Mechanical Engineering, University of California, Santa Barbara, Santa Barbara, CA. His research interests include compliant robot body design, mechanism design, nontraditional materials, artificial muscles, directional adhesion, and growing robots. Dr. Hawkes was the recipient of the NSF CAREER Award in 2020.

Tania K. Morimoto received the B.S. degree from Massachusetts Institute of Technology, Cambridge, MA, in 2012 and the M.S. and Ph.D. degrees from Stanford University, Stanford, CA, in 2015 and 2017, respectively, all in mechanical engineering. She is currently an Assistant Professor of mechanical and aerospace engineering and an Assistant Professor of surgery with University of California, San Diego. Her research interests include robotics, haptics, and engineering education. Dr. Morimoto was the recipient of the NSF CARRER Award in 2022.